

Uniting superhardness and damage-tolerance in a nanosandwich-structured Ti–B–N coating

Jiang Xu,^{a,b,*} ZhengYang Li,^c Zong-Han Xie^{d,e,*} and Paul Munroe^f

^aDepartment of Material Science and Engineering, Nanjing University of Aeronautics and Astronautics, 29 Yudao Street, Nanjing 210016, People's Republic of China

^bSchool of Mechanical & Electrical Engineering, Wuhan Institute of Technology, 693 Xiongchu Avenue, Wuhan 430073, People's Republic of China

^cInstitute of Mechanics, Chinese Academy of Sciences, Beijing 100190, People's Republic of China

^dSchool of Mechanical Engineering, University of Adelaide, SA 5005, Australia

^eSchool of Engineering, Edith Cowan University, Joondalup WA6027, Australia

^fSchool of Materials Science and Engineering, University of New South Wales, NSW 2052, Australia

Received 3 October 2013; revised 2 November 2013; accepted 4 November 2013

Available online 9 November 2013

A novel nanosandwich-structured Ti–B–N coating was prepared on a Ti–6Al–4V substrate using a double glow discharge plasma technique. This coating consists of alternating Ti(N,B) nanocrystalline layers, containing nanoscale growth twins, and amorphous TiB₂–BN layers. Compared with a monolithic TiB_{2.06} nanocrystalline coating, the new Ti–B–N coating exhibits a marked increase in both damage resistance and hardness (i.e. ~55 GPa). The enhanced mechanical properties were found to stem from a combination of nanostructuring and nanotwinning effects.

© 2013 Acta Materialia Inc. Published by Elsevier Ltd. All rights reserved.

Keywords: Nanocomposite; Surface modification; Mechanical properties; Toughness

Single-phase nitride and boride coatings are now being used to protect a variety of structural engineering materials from wear, corrosion and erosion. However, premature failure of these coatings caused by their relatively low hardness, fracture toughness and thermal stability, which can expose the less strong substrate to dangerous environments, is still an overriding concern [1]. Driven by increasing requirements for industrial applications, the development of advanced coatings with desirable properties has focused on synthesizing multi-elemental and multi-phase structures [2,3]. Among them, superhard coatings, consisting of at least two nanoscale phases with strong chemical segregation, have received considerable attention, because they exhibit superior properties and potential in rectifying the limitations of single-phase hard coatings [4,5]. As one of the most promising multiphase systems, Ti–B–N nanocomposite coatings are attractive candidates for use in surface protection of metal components under severe loads and in aggressive environments, due to their high hardness, chemical inertness and good thermal stability

at high temperatures [6,7]. Most of the recent studies in this field have concentrated primarily on the effects of chemical composition and post-deposition annealing on the microstructural evolution and hardness of these TiBN coatings [8–10]. Their extremely high hardness was attributed to the small grain size limiting dislocation-mediated deformation and the strong boundary phase inhibiting interfacial sliding. However, with the increasing hardness, low damage tolerance has become a major issue that hinders the wide application of these coatings. There is a lack of a design strategy that can effectively tackle this problem while still maintaining the high hardness of the coatings. In this work, a novel nanosandwich-structured Ti–B–N coating containing nanoscale growth twins was fabricated on a Ti–6Al–4V substrate by a double glow discharge plasma technique. The roles of nanostructuring and growth twins in governing the hardness and damage resistance of the newly developed coating were examined and clarified in comparison to a monolithic TiB_{2.06} nanocrystalline coating.

Ternary Ti–B–N and binary Ti–B coatings were deposited onto polished Ti6Al4V substrates by using a double cathode glow discharge apparatus equipped with

* Corresponding authors. Tel.: +61 883133980; e-mail addresses: xujiang73@nuaa.edu.cn; zonghan.xie@adelaide.edu.au

a $\text{Ti}_{30}\text{B}_{70}$ target. One cathode serves as the target, and is composed of the desired sputtering material, and the other is the substrate material, as described elsewhere [11]. The base pressure in the chamber was 5×10^{-4} Pa, and the working pressure was 35 Pa during depositions. Synthesis of the Ti–B–N coating was conducted in a flowing Ar + N_2 gas mixture, with an Ar: N_2 ratio of 20:1, while the single-phase $\text{TiB}_{2.06}$ coating was grown in Ar gas at a constant flow rate of 25 sccm. All of the coatings were deposited at a target bias voltage of 800 V, a substrate bias voltage of 300 V and a substrate temperature of 650 °C, with a parallel distance between the source and the substrate of 10 mm and a deposition time of 2 h. The crystallographic structure of the coatings was analyzed by Bragg–Brentano X-ray diffraction (XRD; D8ADVANCE) with Cu K_α radiation. Both the elemental concentration and the phase composition of the coatings were determined by X-ray photoelectron spectroscopy (XPS) using a Kratos AXIS Ultra ESCA System with an X-ray source of Al K_α . The quantitative analysis of XPS experimental data was carried out using CasaXPS-Version 2.3.14. After subtracting the background signal, the spectra were fitted by both Gaussian and mixed Gaussian/Lorentzian functions. The relative sensitivity factors for each element were obtained from the standard CasaXPS database. The atomic concentration of each component was calculated based on the percentage area of the component provided by the CasaXPS software. Prior to XPS analyses, the surface of the specimens was sputtered by a 3 keV Ar^+ ion beam for 2 min to remove surface contamination. The coating microstructure was characterized by scanning electron microscopy (Quanta 200, FEI Company) and field emission transmission electron microscopy (Philips CM200, Eindhoven, Netherlands). The hardness and elastic modulus of the coatings were obtained using a nanoindentation tester (Ultra-Micro Indentation System 2000) equipped with a Berkovich indenter [12,13]. Sub-surface sectioning and imaging of indentation sites created at 500 mN were carried out using a dual electron/focused ion beam system (Nova Nanolab 200, FEI Company) [14,15].

According to the relative atomic concentration calculated from the $\text{Ti}2p$, $\text{B}1s$ and $\text{N}1s$ XPS peak areas, the exact stoichiometries of both the ternary Ti–B–N and binary Ti–B coatings were identified and can be expressed in the form $\text{TiB}_{2.2}\text{N}_{1.3}$ and $\text{TiB}_{2.06}$. On the basis of the Ti–B–N phase diagram [3], the phase composition of the $\text{TiB}_{2.2}\text{N}_{1.3}$ coating should lie within a three-phase region containing TiB_2 , TiN and BN. As shown in Figure 1(a), the $\text{TiB}_{2.06}$ coating exhibits a single $\text{B}1s$ peak at 187.8 eV, corresponding to TiB_2 [16]. This indicates that only TiB_2 phase exists in the $\text{TiB}_{2.06}$ coating. The $\text{B}1s$ spectrum of the $\text{TiB}_{2.2}\text{N}_{1.3}$ coating consists of two $\text{B}1s$ components, with $\text{B}1s$ peak positions located at binding energies of 187.8 and 190.5 eV, which correspond to TiB_2 and BN, respectively [16]. Figure 1(b) shows the XPS core-electron level $\text{Ti}2p$ spectra recorded from the two coatings. The $\text{Ti}2p$ spectrum for the $\text{TiB}_{2.06}$ coating exhibits a single $\text{Ti}2p_{3/2}$ peak located at a binding energy of 455.5 eV, in good agreement with the values obtained for TiB_2 [17]. For the $\text{TiB}_{2.2}\text{N}_{1.3}$ coating,

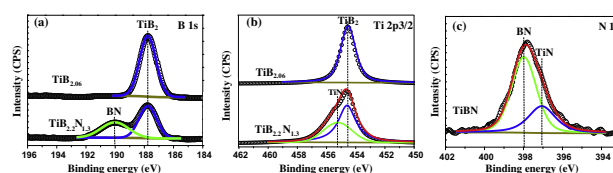


Figure 1. XPS spectra of the (a) $\text{B}1s$, (b) $\text{Ti}2p$ and (c) $\text{N}1s$ core electrons for the two coatings.

$\text{Ti}2p$ peak can be resolved into two main components at 455.5 and 456.7 eV, corresponding to TiB_2 and TiN, respectively. From Figure 1(c), it is found that $\text{N}1s$ peak of the $\text{TiB}_{2.2}\text{N}_{1.3}$ coating can be deconvoluted into two peaks located at 397.2 and 398.1 eV, which are attributable to TiN and BN [18], respectively. By quantitative evaluations of the XPS data, the phase fractions for the $\text{TiB}_{2.2}\text{N}_{1.3}$ coating are derived, i.e. 32.56% TiB_2 , 48.46% BN and 18.98% TiN, respectively [19]. They are consistent with those predicted from the Ti–B–N phase diagram. All the XRD peaks of the $\text{TiB}_{2.06}$ coating can be indexed as hexagonal TiB_2 (JCPDS No.75-1045; see Fig. S1 in the Supplemental material). The XRD pattern of $\text{TiB}_{2.2}\text{N}_{1.3}$ coating, however, exhibits three characteristic TiN peaks (JCPDS No.38-1420), appearing at 2θ angles of 36.5, 42.5 and 61.7°, which can be assigned respectively to the (111), (200) and (220) planes of face-centered cubic (fcc) B1–NaCl-structured TiN. In contrast to the XPS measurements, characteristic diffraction peaks were not detected from either TiB_2 or BN, suggesting that both phases exist in an amorphous state. Moreover, the $\text{TiB}_{2.2}\text{N}_{1.3}$ coating shows a preferred TiN (200) orientation. This phenomenon results presumably from the incorporation of B into the TiN lattice [7]. It has been reported that the addition of B can promote the transformation of the preferred orientation of as-prepared TiN films from (111) to (200) [20]. The two coatings have a thickness of $\sim 10 \mu\text{m}$ and exhibit a dense and homogeneous structure (see Fig. S2 in the Supplemental material). They are tightly adhered to the Ti–6Al–4V substrate without pores, cavities or microcracks visible at the interface between the coating and the substrate.

As shown in Figure 2(a) and (b), the $\text{TiB}_{2.06}$ coating has a polycrystalline structure composed of equiaxed grains of different orientations. The grain size of the crystallites is about 5–11 nm, with an average value of about 8 nm, calculated from crystallites evident in dark-field images. Numerous lattice fringes can be observed in the high-resolution transmission electron microscopy (HRTEM) image for $\text{TiB}_{2.06}$ coating (Fig. 2(b)). The space of the lattice fringes marked as A and B were calculated respectively as 2.63 and 2.04 Å, which correspond to the spacing of the (100) and (101) planes of TiB_2 . The excess B in the overstoichiometric $\text{TiB}_{2.06}$ coating is supposed to segregate to the boundaries of TiB_2 grains, forming disordered B-rich regions [21]. In comparison, the $\text{TiB}_{2.2}\text{N}_{1.3}$ coating is characterized by a unique sandwich-like structure (Fig. 2(c)), wherein vertically aligned, alternating thick and thin layers are bonded closely to one another (see the upper right inset in Fig. 2(c)). The thick layers with a featureless contrast are made of an amorphous phase, as indicated by a diffused halo shown in the selected area

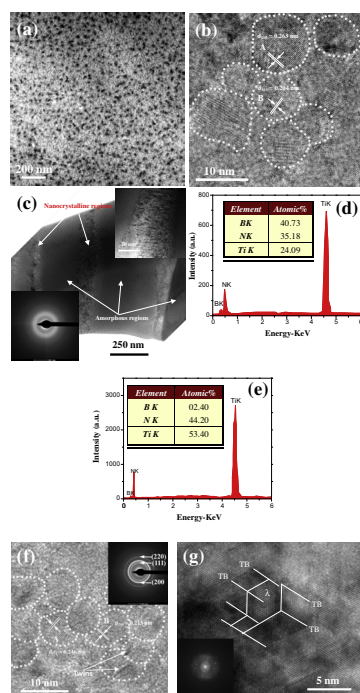


Figure 2. Typical plan-view bright-field TEM (a) and HRTEM (b) images of the $\text{TiB}_{2.06}$ coating; (c) low-magnification bright-field TEM of the $\text{TiB}_{2.2}\text{N}_{1.3}$ coating. The upper right inset in (c) shows the interface between the amorphous and nanocrystalline regions. The lower left inset in (c) shows the SAD pattern of the amorphous regions. EDX analysis from both the amorphous $\text{TiB}_2\text{-BN}$ (d) and nanocrystalline Ti(N,B) regions (e). (f) HRTEM images and corresponding selected area electron diffraction pattern (inset) of the nanocrystalline regions; (g) an HRTEM image of $\text{TiB}_{2.2}\text{N}_{1.3}$ coating showing lamellar nanotwins with a twin thickness of ~ 3.5 nm in nanocrystalline regions; its FFT is inset.

diffraction (SAD) pattern (lower left inset in Fig. 2(c)). The results of energy-dispersive spectroscopic analysis indicate that the amorphous region contains Ti, N and B elements (Fig. 2(d)), whereas the nanocrystalline region is enriched in Ti and N with small amounts of B (Fig. 2(e)). By way of contrast, the thin layers are composed of nanocrystallites with an average grain size of ~ 5 nm in diameter, as shown in Figure 2(f). According to JCPDS data for fcc TiN, the lattice fringes of ~ 2.46 Å in grain A and of ~ 2.13 Å in grain B (Fig. 2(f)) are believed to be those of $\{111\}$ and $\{200\}$ planes of Ti(N,B). In addition, an intense (200) ring in the SAD patterns indicates that the coating exhibits a strong (200)-oriented texture, which is in agreement with the XRD results. It is worth noting that the amorphous/nanocrystalline sandwich architecture of the $\text{TiB}_{2.2}\text{N}_{1.3}$ coating is unique and quite distinct from that of Ti–B–N nanocomposite coating reported by other researchers [7,8], in which individual TiN grains are strongly bonded to one another by a few atomic layers of amorphous phase. Furthermore, HRTEM observations reveal that a high density of nanosized growth twins exist within the Ti(N,B) grains (Fig. 2(g)). The corresponding fast Fourier transformation (FFT) pattern shows a streaking character, indicative of the presence of a large strain in the TiN grains, presumably induced by twin formation. Similar findings have also been reported by Lu et al. [7]. The mechanism

that governs the formation of such an unusual nano-sandwiched structure in the Ti–B–N film remains the subject of an ongoing investigation and is briefly discussed in Section 4 of the Supplementary materials.

The nanoindentation tests (see Fig. S3 in the Supplementary material) show that the values of hardness and elastic modulus of the $\text{TiB}_{2.2}\text{N}_{1.3}$ coating ($H = 55 \pm 0.7$ GPa, $E = 456 \pm 3$ GPa) are significantly higher than those of the $\text{TiB}_{2.06}$ coating ($H = 43 \pm 0.4$ GPa, $E = 397 \pm 7$ GPa). Remarkably, the hardness value of the $\text{TiB}_{2.2}\text{N}_{1.3}$ coating is comparable to the highest hardness value (55 GPa) of the nanostructured Ti–B–N coating consisting of equal fractions of nc-TiN and a- TiB_2 phases prepared by sputter deposition [22], and is greater than the hardness values for the nanocomposite nc-TiN/a-(TiB_2 , BN) thin films synthesized by other techniques [20,23]. Figure 3(a) and (b) presents FIB cross-sectional images of indents in the two coatings, created by a Berkovich diamond tip at 500 mN. Although no cracks are visible from the corners of the indents for the $\text{TiB}_{2.06}$ coating, significant sub-surface cracks can be observed (Fig. 3(a)). As also shown in Figure 3(a), some cracks propagate from the indent edges downward at an acute angle, while cracks below the indentation extend in the direction perpendicular to the sample surface at a greater depth. In contrast, no sub-surface cracks are observed for the $\text{TiB}_{2.2}\text{N}_{1.3}$ coating under the same loading conditions (Fig. 3(b)), meaning that the $\text{TiB}_{2.2}\text{N}_{1.3}$ coating possesses a greater resistance to crack formation. Moreover, it is noteworthy that circular shear bands appear at the indent surfaces of the two coatings, but this is more evident for the $\text{TiB}_{2.2}\text{N}_{1.3}$, as indicated by the arrows. This is a common feature often found in metallic glasses and nanostructured films using instrumented indentation methods [24].

An intriguing question may be asked from the present investigation: why does the nanosandwich-structured $\text{TiB}_{2.2}\text{N}_{1.3}$ coating possess a unique combination of higher hardness and damage tolerance as compared to the monolithic $\text{TiB}_{2.06}$ nanocrystalline coating? As mentioned above, the $\text{TiB}_{2.2}\text{N}_{1.3}$ microstructure consists of vertically aligned, alternating amorphous and nanocrystalline layers. This is distinctly different from the microstructure of Ti–B–N nanocomposite films reported by many researchers, which typically comprises a few-nanometer-scale TiN crystallites embedded in an amorphous phase, a prerequisite for reaching superhardness [5]. For the monolithic $\text{TiB}_{2.06}$ nanocrystalline coating (grain size < 10 nm), because of the absence of dislocation activity in such small crystallites, the deformation mechanism is dominated by grain-boundary shear, resembling shear banding in amorphous

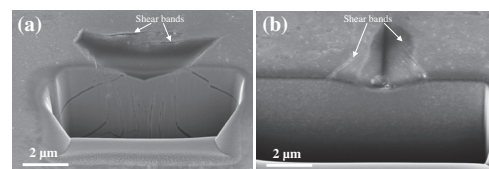


Figure 3. Secondary electron FIB cross-sectional images of indents in the $\text{TiB}_{2.06}$ (a) and $\text{TiB}_{2.2}\text{N}_{1.3}$ (b) coatings subjected to load of 500 mN using a Berkovich diamond tip.

materials [25,26]. Due to the lack of effective work hardening to divert the shear flow, this nanocrystalline coating would undergo inhomogeneous plastic deformation through the formation of highly localized shear bands, which would consequently lead to premature catastrophic failure [27]. By contrast, the $\text{TiB}_{2.2}\text{N}_{1.3}$ coating exhibits a multiphase heterogeneous microstructure featuring alternating nanocrystalline and amorphous layers. Previous studies have shown that the blending of crystalline phase into a glassy matrix is an effective way to simultaneously enhance strength and ductility [28]. Here, the nanocrystalline layers may assume two distinct roles: on the one hand, they provide geometrical confinement against the propagation of shear bands in the amorphous layers and, on the other hand, they promote the formation of multiple shear bands within themselves, corroborated by appearance of numerous shear bands seen in Figure 3(b) [29,30]. Additionally, inside the nanocrystalline layers exists a high density of nanoscale growth twins with a twin thickness of ~ 3.5 nm. Several studies have indicated that, by decreasing the twin thickness in nanotwinned metals, more space is created for the storage of dislocations, giving rise to pronounced strain hardening results [31,32]. For example, Lu et al. [32] found that, when the twin thickness is less than 15 nm, the strain hardening behavior of nanotwinned Cu is governed predominantly by dislocation–twin boundary interactions, resulting in a substantial increase in tensile ductility. Recently, Tian et al. [33] reported that, by decreasing the twin thickness down to 3.8 nm, the hardness and toughness of the nanotwinned c-BN increases significantly, due to a quantum confinement effect and multiple parallel laminated nanotwins being formed at the sub-grain level. Therefore, in the present study, such a nanosandwich structure, together with nanoscale growth twins, is capable of imparting the $\text{TiB}_{2.2}\text{N}_{1.3}$ coating with a striking combination of high hardness and damage resistance.

In summary, a novel nanosandwich-structured Ti–B–N coating was deposited on a Ti–6Al–4V substrate by a double glow discharge plasma technique. The newly developed coating consists of vertically aligned, alternating nanocrystalline Ti(N,B) and amorphous TiB_2 –BN layers. It exhibits extremely high hardness, due in part to the nanotwinned substructure and a quantum confinement effect. To render the coating highly damage tolerant, the nanocrystalline layers act as a physical barrier that suppresses shear band propagation in the adjacent layers while, at the same time, facilitating the formation of controlled shear bands within themselves. In addition, nanoscale growth twins in the nanocrystalline layers play a part in enhancing the ductility of the Ti–B–N coating. Consequently, the Ti–B–N coating exhibits a unique combination of high hardness and damage tolerance in comparison to the monolithic $\text{TiB}_{2.06}$ nanocrystalline coating. It is anticipated that the newly developed coating could be used for safety-critical applications where catastrophic failure is not tolerated.

The authors acknowledge the financial support of the National Natural Science Foundation of China under Grant No. 51374130 and the Aeronautics Science Foundation of China under Grant No. 2013ZE52058.

Supplementary data associated with this article can be found, in the online version, at <http://dx.doi.org/10.1016/j.scriptamat.2013.11.004>.

- [1] C.L. Yeh, G.S. Teng, *J. Alloys Compd.* 417 (2006) 109.
- [2] Y.H. Lu, Y.G. Shen, *Appl. Phys. Lett.* 90 (2007) 221913.
- [3] M.A. Baker, C. Rebholz, A. Leyland, A. Matthews, *Vacuum* 67 (2002) 471.
- [4] P.H. Mayrhofer, C. Mitterer, L. Hultman, H. Clemens, *Prog. Mater. Sci.* 51 (2006) 1032.
- [5] S. Veprek, M.G.J. Veprek-Heijman, P. Karvankova, J. Prochazka, *Thin Solid Films* 476 (2005) 1.
- [6] P.H. Mayrhofer, M. Stoiber, C. Mitterer, *Scr. Mater.* 53 (2005) 241.
- [7] Y.H. Lu, Z.J. Liu, Y.G. Shen, *Acta Mater.* 54 (2006) 2897.
- [8] Y.H. Lu, Z.K. Xu, H. Chen, Y.G. Shen, K.Y. Li, *Appl. Phys. Lett.* 87 (2005) 151902.
- [9] L. Garcia-Gonzalez, J. Hernandez-Torres, P.J. Garcia-Ramirez, J. Martinez-Castillo, A. Saucedo, A.L. Herrera-May, F.J. Espinoza-Beltran, *J. Mater. Process. Technol.* 186 (2007) 362.
- [10] P.H. Mayrhofer, C. Mitterer, J.G. Wen, I. Petrov, J.E. Greene, *J. Appl. Phys.* 100 (2006) 044301.
- [11] J. Xu, D. Lai, Z.H. Xie, P. Munroe, Z.T. Jiang, *J. Mater. Chem.* 22 (2012) 2596.
- [12] M.S. Ahmed, X.L. Zhao, Z.F. Zhou, P. Munroe, N.C. Tan, K.Y. Li, Z.H. Xie, *J. Am. Ceram. Soc.* 94 (2011) 1546.
- [13] Z.H. Xie, M.V. Swain, M.J. Hoffman, *J. Dent. Res.* 88 (2009) 529.
- [14] Z.H. Xie, R.J. Moon, M. Hoffman, P. Munroe, Y.B. Cheng, *J. Eur. Ceram. Soc.* 23 (2003) 2351.
- [15] Z.H. Xie, P.R. Munroe, R.J. Moon, M. Hoffman, *Wear* 255 (2003) 651.
- [16] M.A. Baker, T.P. Mollart, P.N. Gibson, W. Gissler, *J. Vac. Sci. Technol., A* 15 (1997) 284.
- [17] S. Seal, T.L. Barr, N. Sobczak, E. Benko, *J. Vac. Sci. Technol., A* 15 (1997) 505.
- [18] C. Ruby, R. Ott, F. Huang, M.L. Weaver, J.A. Barnard, *Surf. Interface Anal.* 29 (2000) 823.
- [19] M.A. Baker, *Surf. Coat. Technol.* 201 (2007) 6105.
- [20] Y.H. Lu, Y.G. Shen, J.P. Wang, Z.F. Zhou, K.Y. Li, *Surf. Coat. Technol.* 201 (2007) 7368.
- [21] P.H. Mayrhofer, C. Mitterer, J.G. Wen, J.E. Greene, I. Petrov, *Appl. Phys. Lett.* 86 (2005) 131909.
- [22] P. Hammer, A. Steiner, R. Villa, M. Baker, P.N. Gibson, J. Haupt, W. Gissler, *Surf. Coat. Technol.* 68 (69) (1994) 194–198.
- [23] G. Bolelli, V. Cannillo, L. Lusvardi, F.P. Mantini, E. Gualtieri, C. Menozzi, *Mater. Lett.* 62 (2008) 1557.
- [24] J.R. Trelewicz, C.A. Schuh, *Acta Mater.* 55 (2007) 5948.
- [25] H. Conrad, J. Narayan, *Acta Mater.* 50 (2002) 67.
- [26] G. He, J. Eckert, W. Loeser, L. Schultz, *Nat. Mater.* 2 (2003) 33.
- [27] C.C. Hays, C.P. Kim, W.L. Johnson, *Phys. Rev. Lett.* 84 (2000) 2901.
- [28] A.T. Alpas, J.D. Embury, *Scr. Metall.* 22 (1988) 265.
- [29] A.L. Greer, Y.Q. Cheng, E. Ma, *Mater. Sci. Eng., R* 74 (2013) 71.
- [30] M. Dao, L. Lu, Y. Shen, S. Suresh, *Acta Mater.* 54 (2006) 5421.
- [31] T. Zhu, J. Li, A. Samanta, H.G. Kim, S. Suresh, *Proc. Natl. Acad. Sci. USA* 104 (2007) 3031.
- [32] L. Lu, X. Chen, X. Huang, K. Lu, *Science* 323 (2009) 607.
- [33] Y.J. Tian, B. Xu, D.L. Yu, Y.M. Ma, Y.B. Wang, Y.B. Jiang, W.T. Hu, C.C. Tang, Y.F. Gao, K. Luo, Z.S. Zhao, L.M. Wang, B. Wen, J. He, Z.Y. Liu, *Nature* 493 (2013) 385.